

Time-dependent numerical renormalization group method for multiple quenches: towards exact results for the long time limit of thermodynamic observables and spectral functions

H. T. M. Nghiem^{1,2} and T. A. Costi¹

¹*Peter Grünberg Institut and Institute for Advanced Simulation, Research Centre Jülich, 52425 Jülich, Germany*

²*Advanced Institute for Science and Technology, Hanoi University of Science and Technology, 10000 Hanoi, Vietnam*

(Dated: December 14, 2024)

We develop an alternative time-dependent numerical renormalization group formalism (TDNRG) for multiple quenches and implement it to study the response of a quantum impurity system to a general pulse. Within this approach, we reduce the contribution of the NRG approximation to numerical errors in the time evolution of observables by a formulation that uses the difference of eigenvalues instead of their absolute values, as in our previous multiple-quench TDNRG formalism [Nghiem *et al.*, Phys. Rev. B **89**, 075118 (2014); Phys. Rev. B **90**, 035129 (2014)]. We demonstrate that the new formalism yields a smaller cumulative error in the trace of the projected density matrix as a function of time and a smaller discontinuity of local observables between quenches than in our previous approach. Moreover, by increasing the switch-on time, the time between the first and last quench of the discretized pulse, the long time limit of observables systematically converges to its expected value in the final state, i.e., the more adiabatic the switching, the more accurately is the long time limit recovered. The present formalism can be straightforwardly extended to infinite switch-on times. We show that this yields highly accurate results for the long time limit of both thermodynamic observables and spectral functions, and overcomes the significant errors within the single quench formalism [Anders *et al.*, Phys. Rev. Lett. **95**, 196801 (2005); Nghiem *et al.*, Phys. Rev. Lett. **119**, 156601 (2017)]. This improvement provides a first step towards an accurate description of nonequilibrium steady states of quantum impurity systems, e.g., within the scattering states NRG approach [Anders, Phys. Rev. Lett. **101**, 066804 (2008)].

I. INTRODUCTION

The response of strongly correlated quantum impurity systems to quenches, pulses, static and time-dependent fields, remains a challenging theoretical topic of relevance to a number of fields, including, low energy ion-surface scattering^{1,2}, time dependent dynamics and pumping in quantum dots^{3–6}, pump-probe spectroscopies of correlated electron materials^{7–10}, and to proposed cold atom realizations of Anderson and Kondo impurity models^{11–14}.

Techniques currently being used to investigate the time-dependent dynamics of quantum impurity systems, include functional and real-time renormalization group methods^{15–17}, flow equation^{18,19}, quantum Monte Carlo^{20–23}, and density matrix renormalization group methods^{24–26}, the hierarchical quantum master equation approach^{27,28}, and the time-dependent numerical renormalization group (TDNRG) method^{29–38}. However, no single technique is able to address in a nonperturbative and numerically exact way the time-dependent and nonequilibrium dynamics of quantum impurity systems in the interesting low temperature strong coupling regime. For example, quantum Monte Carlo approaches become numerically expensive in the zero temperature limit²¹, the functional renormalization group approach, while versatile, is often only quantitatively accurate for weak to intermediate interaction strengths^{15,39} and the (single-quench) TDNRG approach suffers from imperfect thermalization and finite errors in the long time limit of observables due, primarily, to the logarithmic discretization of the bath inherent to this approach^{30–33,35–38,40}. Nevertheless, an approach for the response of quantum impurity systems to time-dependent fields based on the latter technique remains promising since it automatically builds in the nonperturbative element of Wilson’s (equilibrium) numerical renormalization group method^{41–44}.

Such an approach would therefore be highly suitable for accessing the low temperature strong coupling physics of quantum impurity models.

In previous work^{35,36}, we proposed to improve the long time limit of thermodynamic observables, following a switch from an arbitrary initial state to an arbitrary final state, within the TDNRG approach, by replacing a single quench by a sequence of n smaller quenches acting over a finite time $\tilde{\tau}_n$ (the switch-on time) within a multiple-quench generalization of the single-quench TDNRG approach. Within such an approach, which also generalizes the TDNRG approach to general pulses and periodic driving, we showed that the long time limit of thermodynamic observables could be systematically improved by increasing the number of quenches and the switch-on time. This resulted in a significant improvement for the long time limit of observables over the corresponding single-quench TDNRG results^{35,36}. Despite this improvement, the approach still suffers from a number of problems, which we outline below, and which, to a large extent, we overcome in this paper, in which we develop a new alternative formulation of the multiple-quench TDNRG approach.

We identify several problems in the time evolution of observables as calculated within our previous multiple-quench TDNRG formalism for general pulses^{35,36} (see Secs. II–III for more details); (i), the trace of the projected density matrix was found to deviate increasingly away from 1 with increasing switch-on time $\tilde{\tau}_n$, the time required to switch from the initial to the final state, up to some finite switch-on time, before decreasing again for longer switch-on times (with a maximum deviation, however, below 1%), (ii), the time evolution of an observable exhibited small discontinuities at the times corresponding to all but the first quench, and, (iii), there was no easy way, within this formalism, to extract, other than numerically, the limit of an infinite switch-on time $\tilde{\tau}_n \rightarrow \infty$. The

problems (i) and (ii) stem from the way the NRG approximation is implemented within this approach and the same problems are also encountered within a hybrid TDNRG approach to periodic switching³³. As for (iii), having a formulation which allows the limit $\tilde{\tau}_n \rightarrow \infty$ to be taken analytically would be advantageous for the following reason: we found in the approach of Ref. 35 and 36 that the dependence of the long time limit of an observable $O(t \rightarrow \infty)$ on $\tilde{\tau}_n$ was, in general, non-monotonic. While $O(t \rightarrow \infty)$ eventually converged with increasing $\tilde{\tau}_n$ to its correct value in the final state for sufficiently large $\tilde{\tau}_n$, it was not a priori evident how large $\tilde{\tau}_n$ should be for convergence to be achieved. This problem is overcome by our new formulation, which allows the limit $\tilde{\tau}_n \rightarrow \infty$ to be taken analytically. In addition, the new formulation yields a much faster convergence of $O(t \rightarrow \infty)$ with increasing $\tilde{\tau}_n$, which is moreover monotonic (see Fig. 3(b) in Sec. III).

In this paper, we present an alternative TDNRG formalism for multiple quenches which largely overcomes the above problems, i.e., (i), the trace of the projected density matrix versus $\tilde{\tau}_n$ remains significantly closer to 1 for all $\tilde{\tau}_n$ (Figs. 2 and 3 in Sec. III), (ii), observables exhibit significantly smaller discontinuities after each quench (Fig. 2(c) in Sec. III), and, (iii), the limit of infinite switch-on times can be taken analytically within this formalism and allows obtaining the long time limit of thermodynamic observables with high accuracy (Sec. IV).

Extending this formalism to spectral functions, we also recover the expected long time value of the spectral function in the equilibrium final state with high accuracy (see Fig. 4 in Sec. IV A). Within a scattering states approach to nonequilibrium steady states^{31,32}, such a calculation would allow the low-temperature nonequilibrium steady-state spectral function and conductance of interacting quantum dots to be calculated accurately for arbitrary bias and gate voltages. Besides the relevance of this for experiments on quantum dots^{45–47}, it would also go beyond the recent exact Fermi liquid approach which addresses only the low bias voltage regime (relative to the Kondo scale)⁴⁸ and could serve as a useful benchmark for other approaches^{20,49–52}.

The outline of the paper is as follows: In section II, the alternative multiple quench TDNRG formalism is derived for finite switch-on times to reduce the effect of the NRG approximation by only using the difference of eigenvalues instead of their absolute values as in Ref. 35 and 36. The improvement is shown by comparing calculations from the two formalisms for the resonant level model and the Anderson impurity model in Sec. III. In section IV, the (straight forward) extension to infinite switch-on times is derived from the formalism presented in Sec. II. Applications are made to the long time limit of the spectral function in Sec. IV A, with additional supporting results in Appendix B, and to thermodynamic observables (occupation and double occupation) in Sec. IV B with comparison of the results to the their expected values in the equilibrium final state. In addition, we show in Sec. IV C results for the occupation number of the resonant level model calculated within exact diagonalization (ED) for multiple quenches in the infinite switch-on time limit, which further support the conclusions made within the multiple quench TDNRG formalism. The TDNRG expression for the spectral function for

multiple quenches, for a finite and infinite switch-on time, is derived in Appendix A. Results for the switch-on time dependence of the spectral function are presented in Appendix C, while Appendix D discusses the effect of different discretization parameters on the error in the projected density matrices. Finally, Appendix E presents the generalization of ED to study the time evolution of a system following multiple quenches with both finite and infinite switch-on times for the exactly solvable resonant level model.

II. MULTIPLE QUENCH TDNRG FOR GENERAL PULSES: ALTERNATIVE FORMALISM

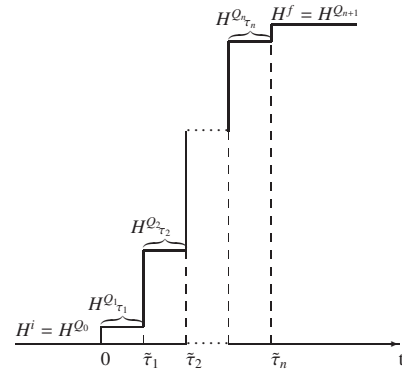


FIG. 1. A system driven from an initial to a final state via a sequence of quantum quenches at times $\tilde{\tau}_0 = 0, \tilde{\tau}_1, \dots, \tilde{\tau}_n$ with evolution according to $\{H^{Q_p}\}$ in the time step $\tilde{\tau}_{p-1} \leq t < \tilde{\tau}_p$ with $H^{Q_0} = H^i$ and $H^{Q_{n+1}} = H^f$. The time, $\tilde{\tau}_n = \sum_{p=1}^n \tau_p$, to switch from H^i to H^f via the sequence of quantum quenches will be called the switch-on time (or, equivalently the pulse duration).

We consider a system driven from an initial state (described by H^i) to a final state (described by H^f) in a time interval $[0, \tilde{\tau}_n]$ via a sequence of $n+1$ quantum quenches described by $H^{Q_p}, p = 1, \dots, n+1$, switched on at times $\tilde{\tau}_{p-1}, p = 1, \dots, n+1$ (with $\tilde{\tau}_0 = 0$) and having duration τ_p (except for $H^{Q_{p=n+1}} = H^f$ which acts for all $t > \tilde{\tau}_n$) as depicted in Fig. 1. The time to switch from the initial to the final state, $\tilde{\tau}_n$, will be referred to as the switch-on time throughout the paper (equivalently, this can be called the duration of the pulse).

The Hamiltonians, $H^{Q_p}, p = 1, \dots, n+1$, will represent an Anderson impurity model $H(t)$ for $\tilde{\tau}_{p-1} \leq t < \tilde{\tau}_p$, with

$$H(t) = H_{\text{imp}} + H_{\text{bath}} + H_{\text{int}}.$$

Here, $H_{\text{imp}} = \sum_{\sigma} \varepsilon_d(t) n_{d\sigma} + U(t) n_{d\uparrow} n_{d\downarrow}$ describes an impurity with a local level of energy $\varepsilon_d(t)$ and a Coulomb repulsion $U(t)$ between opposite spin electrons in the local level. The impurity interacts with free conduction electrons described by $H_{\text{bath}} = \sum_{k\sigma} \varepsilon_{k\sigma} c_{k\sigma}^{\dagger} c_{k\sigma}$ via a hybridization interaction $H_{\text{int}} = V \sum_{k\sigma} (c_{k\sigma}^{\dagger} d_{\sigma} + h.c.)$. The time dependence enters through either a time dependent level position $\varepsilon_d(t)$ or a time dependent Coulomb repulsion $U(t)$ and will be specified in detail for each switching protocol later. We shall consider a time-independent hybridization V throughout this paper, and

we shall denote the constant single-particle broadening of the resonant level by $\Gamma = \pi\rho V^2$, where $\rho = 1/2D$ is the constant density of states per spin of the conduction electrons and $D = 1$ is the half bandwidth.

The quench Hamiltonians, $H^{Q_p}, p = 1, \dots, n+1$, are solved by using Wilson's NRG approach^{42,44} to yield the eigenstates and eigenvalues of each quench Hamiltonian at each NRG iteration $m = m_0, \dots, N$, where N is the longest chain diagonalized and m_0 (typically 6 or 7) is the first iteration at which high energy states are discarded. In the iterative diagonalization of the Hamiltonians $H^{Q_p}, p = 1, \dots, n+1$ we retain either of order $N_s = 1000$ states per iteration or truncate the spectrum at a fixed energy $E_{\text{cut}} = 24$ (measured in units of the characteristic scale $t_m \sim \Lambda^{-(m-1)/2}$ of the m -th truncated Hamiltonian $H_m^{Q_p}$, where $\Lambda > 1$ is the logarithmic discretization parameter⁴⁴). We make use of the complete basis set of discarded states²⁹ $\{|l_p e_p m_p\rangle_{Q_p}\}$ of H^{Q_p} where l_p labels the eigenstate, e_p the environment variable and m_p the truncated Hamiltonian at NRG iteration $m = m_p$ and the following decomposition of unity applies

$$\sum_{l_p e_p m_p} |l_p e_p m_p\rangle_{Q_p} \langle l_p e_p m_p| = 1.$$

In addition, in evaluating thermodynamic expectation values of observables, we used the full density matrix representation⁵³ for the initial state density matrix ρ of H^i and the z-averaging procedure^{54,55} to reduce discretization effects.

With the above preliminaries, we can now write down the time evolution $O(t)$ of a local observable \hat{O} at time $t \in [\tilde{\tau}_p, \tilde{\tau}_{p+1})$. In the notation of Ref. 35 and 36 we have

$$O(t) = \sum_{m_{p+1} l_{p+1} e_{p+1}} \mathcal{Q}_{p+1} \langle l_{p+1} e_{p+1} m_{p+1} | e^{-iH^{Q_{p+1}}(t-\tilde{\tau}_p)} e^{-iH^{Q_p} \tau_p} \dots e^{-iH^{Q_1} \tau_1} \times \rho e^{iH^{Q_1} \tau_1} \dots e^{iH^{Q_p} \tau_p} e^{iH^{Q_{p+1}}(t-\tilde{\tau}_p)} \hat{O} | l_{p+1} e_{p+1} m_{p+1} \rangle_{Q_{p+1}}, \quad (1)$$

with ρ the full density matrix⁵³ of the initial state Hamiltonian H_i at inverse temperature $\beta = 1/T$. For the simplest case with $\tilde{\tau}_1 > t \geq \tilde{\tau}_0$, the single quench result for $O(t)$ applies²⁹. For the next simplest case with $\tilde{\tau}_2 > t \geq \tilde{\tau}_1$, we have

$$O(t) = \sum_{m_2 l_2 e_2} \mathcal{Q}_2 \langle l_2 e_2 m_2 | e^{-iH^{Q_2}(t-\tilde{\tau}_1)} e^{-iH^{Q_1} \tau_1} \times \rho e^{iH^{Q_1} \tau_1} e^{iH^{Q_2}(t-\tilde{\tau}_1)} \hat{O} | l_2 e_2 m_2 \rangle_{Q_2} = \sum_{m_2 l_2 e_2} \sum_{m'_2 l'_2 e'_2} \sum_{m_1 l_1 e_1} \sum_{m'_1 l'_1 e'_1} \mathcal{Q}_2 \langle l_2 e_2 m_2 | e^{-iH^{Q_2}(t-\tilde{\tau}_1)} | l_1 e_1 m_1 \rangle_{Q_1} \times \mathcal{Q}_1 \langle l_1 e_1 m_1 | e^{-iH^{Q_1} \tau_1} \rho e^{iH^{Q_1} \tau_1} | l'_1 e'_1 m'_1 \rangle_{Q_1} \times \mathcal{Q}_1 \langle l'_1 e'_1 m'_1 | e^{iH^{Q_2}(t-\tilde{\tau}_1)} | l'_2 e'_2 m'_2 \rangle_{Q_2} \mathcal{Q}_2 \langle l'_2 e'_2 m'_2 | \hat{O} | l_2 e_2 m_2 \rangle_{Q_2},$$

where three decompositions of unity $1 = \sum_{l e m} |l e m\rangle \langle l e m|$ have been employed. Next, we use the identity⁵⁶

$$\sum_{m_2 l_2 e_2} \sum_{m'_2 l'_2 e'_2} \sum_{m_1 l_1 e_1} \sum_{m'_1 l'_1 e'_1} = \sum_m \sum_{e_1 e'_1 e_2 e'_2} \sum_{r_1 s_1 r_2 s_2} \quad (2)$$

to convert the multiple-shell sums over the four different Wilson chains in the above expression for $O(t)$ into a single shell-diagonal (restricted) sum involving kept states ($K_1 K'_1$ etc³⁰), obtaining

$$\begin{aligned} O(t) &= \sum_m \sum_{r_1 s_1 r_2 s_2} \sum_{e_1 e'_1 e_2 e'_2} \mathcal{Q}_2 \langle r_2 e_2 m | e^{-iH^{Q_2}(t-\tilde{\tau}_1)} | r_1 e_1 m \rangle_{Q_2} \\ &\quad \times \mathcal{Q}_1 \langle r_1 e_1 m | e^{-iH^{Q_1} \tau_1} \rho e^{iH^{Q_1} \tau_1} | s_1 e'_1 m \rangle_{Q_1} \\ &\quad \times \mathcal{Q}_1 \langle s_1 e'_1 m | e^{iH^{Q_2}(t-\tilde{\tau}_1)} | s_2 e'_2 m \rangle_{Q_2} \mathcal{Q}_2 \langle s_2 e'_2 m | \hat{O} | r_2 e_2 m \rangle_{Q_2} \\ &= \sum_m \sum_{r_1 s_1 r_2 s_2} S_{r_2 r_1}^m \sum_e \mathcal{Q}_1 \langle r_1 e m | \rho | s_1 e m \rangle_{Q_1} e^{-i(E_{r_1}^m - E_{s_1}^m) \tau_1} \\ &\quad \times S_{s_1 s_2}^m O_{s_2 r_2}^m e^{-i(E_{r_2}^m - E_{s_2}^m) (t-\tilde{\tau}_1)} \\ &= \sum_m \sum_{r_1 s_1 r_2 s_2} S_{r_2 r_1}^m \rho_m^{i \rightarrow Q_1} (r_1, s_1) e^{-i(E_{r_1}^m - E_{s_1}^m) \tau_1} \\ &\quad \times S_{s_1 s_2}^m O_{s_2 r_2}^m e^{-i(E_{r_2}^m - E_{s_2}^m) (t-\tilde{\tau}_1)}. \end{aligned} \quad (3)$$

Here, $S_{r_2 r_1}^m$ is the overlap matrix element which is defined as $S_{r_2 r_1}^m \times \delta_{e_2, e_1} = \mathcal{Q}_2 \langle r_2 e_2 m | r_1 e_1 m \rangle_{Q_1}$, $O_{s_2 r_2}^m$ is the matrix elements of \hat{O} that $O_{s_2 r_2}^m \times \delta_{e'_2, e_2} = \mathcal{Q}_2 \langle s_2 e'_2 m | \hat{O} | r_2 e_2 m \rangle_{Q_2}$, and $\rho_m^{i \rightarrow Q_1} (r_1, s_1) = \sum_e \mathcal{Q}_1 \langle r_1 e m | \rho | s_1 e m \rangle_{Q_1}$ is the reduced initial state density matrix (of H_i) projected onto the state of H^{Q_1} ³⁵. Furthermore, in the second line of Eq. (3), use has been made of the NRG approximation in the form $e^{iH^{Q_1} \tau_1} |r_1 e_1 m\rangle_{Q_1} \approx e^{iE_{r_1}^m \tau_1} |r_1 e_1 m\rangle_{Q_1}$, which, except in the limit of a vanishing switch-on time $\tau_1 = 0$, incurs a finite error in the time evolution, so Eq. (3) should be understood as being approximate.

For the general case with $t \in [\tilde{\tau}_p, \tilde{\tau}_{p+1})$, we obtain, by using a generalization of Eq. (2)⁵⁶,

$$\begin{aligned} O(t) &= \sum_m \sum_{r_1 s_1 \dots r_p s_p r_{p+1} s_{p+1}} S_{r_{p+1} r_p}^m \dots S_{r_2 r_1}^m \rho_m^{i \rightarrow Q_1} (r_1, s_1) \\ &\quad \times e^{-i(E_{r_1}^m - E_{s_1}^m) \tau_1} S_{s_1 s_2}^m \dots e^{-i(E_{r_p}^m - E_{s_p}^m) \tau_p} S_{s_p s_{p+1}}^m \\ &\quad \times O_{s_{p+1} r_{p+1}}^m e^{-i(E_{r_{p+1}}^m - E_{s_{p+1}}^m) (t-\tilde{\tau}_p)}, \end{aligned} \quad (4)$$

where, again, the use of the NRG approximation, implies that this expression should be understood, in general, as being approximate. When $p = n$, Eq. (4) applies for all $t \geq \tilde{\tau}_n$, and can be used to extract the long time limit $t \rightarrow \infty$ of observables, both for a finite or an infinite switch-on time $\tilde{\tau}_n$. Below, we shall discuss the accuracy of the long time limit of observables $O(t \rightarrow \infty)$ as a function of the switch-on time $\tilde{\tau}_n$ (or, equivalently the pulse duration). For zero switch-on time, $\tilde{\tau}_n = 0$ (or equivalently $\tau_1 = \tau_2 = \dots = \tau_p = 0$), the above expression can be converted into that for a single quench³⁵.

For the special case that \hat{O} is the identity operator, $\hat{O} = \hat{I}$, we have

$$\begin{aligned} 1 &= \sum_m \sum_{r_1 s_1 \dots r_p s_p r_{p+1}} S_{r_{p+1} r_p}^m \dots S_{r_2 r_1}^m \rho_m^{i \rightarrow Q_1} (r_1, s_1) \\ &\quad \times e^{-i(E_{r_1}^m - E_{s_1}^m) \tau_1} S_{s_1 s_2}^m \dots e^{-i(E_{r_p}^m - E_{s_p}^m) \tau_p} S_{s_p s_{p+1}}^m. \end{aligned} \quad (5)$$

The right hand side of this expression depends on time in a stepwise fashion through the restriction that $t \in [\tilde{\tau}_p, \tilde{\tau}_{p+1}]$. The above expression should, in general, be understood as approximate due to the use of the NRG approximation in its derivation. Equation (5) is analogous to the trace of the projected density matrix defined in Refs. 35 and 36, therefore the calculation of $\langle \hat{I} \rangle$ by using this equation will be referred to in the following as the trace of the projected density matrix, and will be denoted by $Tr[\rho^{i \rightarrow f}(t)]$ with $t \in [\tilde{\tau}_p, \tilde{\tau}_{p+1}]$. For $t > \tilde{\tau}_n$, it is independent of time and denoted by $Tr[\rho^{i \rightarrow f}(\tilde{\tau}_n)]$. The deviation of $Tr[\rho^{i \rightarrow f}(\tilde{\tau}_n)]$ from 1 represents the cumulative error in the trace due to the NRG approximation and will be investigated in detail in the next section. In the limit of a vanishing switch-on time, equivalent to a single quench, the NRG approximation is inoperative and the resulting expression $1 = Tr[\rho^{i \rightarrow Q_1}]$ is satisfied exactly, as shown explicitly in Ref. 35.

Since we also wish to compare the present formalism with our previous multiple quench TDNRG formalism^{35,36}, a few words are in order about the latter. In Refs. 35 and 36, we expressed the time evolution of an observable \hat{O} for $t \in [\tilde{\tau}_p, \tilde{\tau}_{p+1}]$ as

$$O(t) = \sum_{mrs}^{\#KK'} \rho_{rs}^{i \rightarrow Q_{p+1}}(m, \tilde{\tau}_p) e^{-i(E_r^m - E_s^m)(t - \tilde{\tau}_p)} O_{sr}^m, \quad (6)$$

with $\rho_{rs}^{i \rightarrow Q_{p+1}}(m, \tilde{\tau}_p) = \sum_e Q_{p+1} \langle rem | e^{-iH^Q_p \tau_p} \dots e^{-iH^{Q_1} \tau_1} \rho e^{iH^{Q_1} \tau_1} \dots e^{iH^{Q_p} \tau_p} | sem \rangle_{Q_{p+1}}$,

a projected density matrix depending on each time step $\tilde{\tau}_p$ that was calculated recursively in terms of reduced density matrices and the so called *generalized overlap matrix elements* defined as

$$S_{r_i s_Q}^m(\tilde{\tau}_p) \times \delta_{ee'} = \langle rem | e^{iH^{Q_1} \tau_1} \dots e^{iH^{Q_p} \tau_p} | se' m \rangle_{Q_{p+1}}. \quad (7)$$

These generalized overlap matrix elements are also calculated recursively at each time step $\tilde{\tau}_p$ from those at the previous time step $\tilde{\tau}_{p-1}$ and enter in the calculation of the above projected density matrices. In contrast, the formalism presented in this paper evaluates the time evolution in terms of the projected density matrix at the first time step $\rho_m^{i \rightarrow Q_1}(r_1, s_1)$ and the ordinary overlap matrix elements $S_{r_{p+1} r_p}^m$ and bypasses the need for a recursive calculation for quantities entering the expression for $O(t)$. It is therefore numerically more efficient and easier to implement than the approach of Ref. 36. A further difference between the present formalism and that in Refs. 35 and 36 is that in the present formalism only differences of many-body eigenvalues (i.e., excitations) appear in the expression for $O(t)$, whereas in Refs. 35 and 36, absolute eigenvalues (measured relative to an absolute groundstate energy) entered the expressions for the generalized overlap matrix elements. The present formalism therefore avoids the need to explicitly keep track of an absolute ground state energy. Finally, within the multiple quench formalism of Ref. 35 and 36, the limit of infinite switch-on time $\tilde{\tau}_n \rightarrow +\infty$ is impossible to take analytically, and that formalism is restricted to numerical evaluations

at finite switch-on times. Within the present formalism, on the other hand, it becomes straightforward to take this limit (see Sec. IV). This, in turn, allows for an adiabatic switching of the system between an arbitrary initial state and an arbitrary final state, thereby improving the long time limit of observables.

III. COMPARISON WITH THE PREVIOUS APPROACH

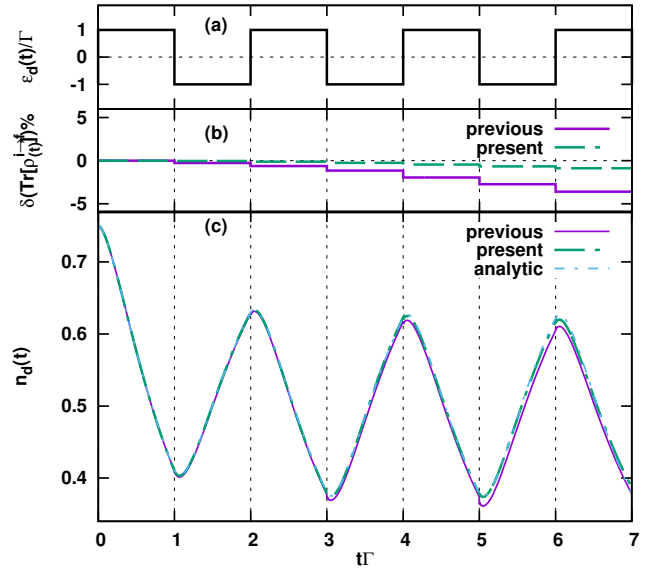


FIG. 2. Results for the resonant level model subject to square periodic driving. (a) The square periodic driving used for $\varepsilon_d(t)/\Gamma$, where $\varepsilon_d(t)$ is the local level position and Γ the hybridization strength in the resonant level model. (b) Percentage deviation, $\delta(Tr[\rho^{i \rightarrow f}(t)])$, of the trace of the projected density matrix away from 1 vs $t\Gamma$ in the present approach (dashed line) and the previous multiple-quench approach of Ref. 36 (solid line). (c) Occupation number $n_d(t)$ vs $t\Gamma$ in the present approach (dashed line), the previous approach (solid line), and, in the exact analytic approach (dash-dotted line). NRG parameters: $\Lambda = 1.6$, the number of kept states in each iteration $N_s = 900$, and $N_z = 16$ values for the z-averaging.

In this section we illustrate the improvement of the present multiple quench TDNRG approach over our previous approach for two specific situations: (i) for the time evolution of the occupation number $\langle n_d(t) \rangle$ in the resonant level model⁵⁷ under a square periodic driving of the local level, and, (ii), for the convergence of the long time limit of the occupation number $\langle n_d(t \rightarrow \infty) \rangle$ with respect to increasing the switch-on time in the interacting Anderson impurity model following a linear ramp of the local level.

In Fig. 2(b), we show the error in $Tr[\rho^{i \rightarrow f}(t)]$ versus time and the time evolution of the occupation number in the resonant level model (RLM) under a square periodic driving of the local level ε_d from $-\Gamma$ to Γ and back with a period of $2/\Gamma$ [Fig. 2(a)]. The results of the present approach are compared with those from our previous multiple-quench formalism in Ref. 36 as well as with the exact analytic result for the RLM. From these comparisons, we see that the previ-

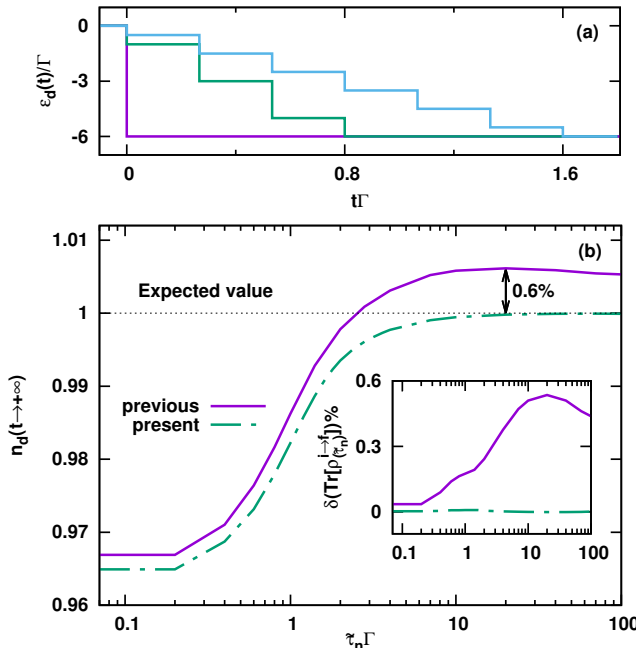


FIG. 3. Anderson model subject to a linear ramp pulse. (a) A single large quench for $\varepsilon_d(t)/\Gamma$ is replaced by a linear ramp pulse and the latter is approximated by a finite sequence of $n > 1$ small quenches of total duration $\tilde{\tau}_n$ (the switch-on time). The system is switched from the mixed valence regime with $\varepsilon_d(t < 0) = 0$ and $U = 12\Gamma$ to the symmetric Kondo regime with $\varepsilon_d(t \geq \tilde{\tau}_n) = -U/2$ and $U = 12\Gamma$ within time $\tilde{\tau}_n$. (b) Occupation number in the long time limit $n_d(t \rightarrow \infty)$ vs $\tilde{\tau}_n\Gamma$ in the present approach (dashed-dotted line) compared to the approach of Ref. 36 (solid line). For each fixed $\tilde{\tau}_n$, the linear ramp pulse is approximated by a sequence of up to 100 small quenches, with the number of quenches chosen such that $n_d(t \rightarrow \infty)$ is converged. The inset shows the corresponding % error in the trace of the projected density matrix $\delta(\text{Tr}[\rho^{i \rightarrow f}(\tilde{\tau}_n)])$ vs $\tilde{\tau}_n\Gamma$ of the present (dot-dashed line) and previous (solid line) multiple-quench approach. NRG parameters: $\Lambda = 4$, $E_{\text{cut}} = 24$, and $N_z = 8$ values for the z-averaging.

ous formalism yields a trace for the projected density matrix ($\text{Tr}[\rho^{i \rightarrow f}(t)]$) which deviates increasingly away from 1 after each quench. Similarly, the discontinuity in the time evolution of the occupation number at the boundaries of the time steps is clearly visible for times $t\Gamma \gtrsim 5$ in the results from the previous formalism. Within the present formalism, the deviation of $\text{Tr}[\rho^{i \rightarrow f}(t)]$ away from 1 is reduced by a factor of more than 10 relative to that in the previous formalism after one period, and the discontinuity in the time evolution of the occupation number also decreases by a similar factor. The present formalism results a time evolution for n_d which is significantly closer to the exact analytic one than that from the previous formalism.

Figure 3 shows results for the Anderson model with a constant Coulomb repulsion $U_i = U_f$ in which the system is switched from the mixed valence regime initially ($\varepsilon_d^i = 0$) to the symmetric Kondo regime in the final state ($\varepsilon_d^f = -U_f/2$): in particular, we show the occupation number in the long time limit $n_d(t \rightarrow \infty)$ and the corresponding % error in the trace

of the projected density matrix as a function of the switch-on time $\tilde{\tau}_n$, comparing the results also with those from our previous approach. We see that $n_d(t \rightarrow \infty)$ initially increases as the switch-on time increases in both approaches. However, while the occupation number in the previous approach eventually overshoots the expected value of 1 in the final state and only begins to drop close to the correct value at very long switch-on times, the present approach converges monotonically to the correct value already at relatively short switch-on times without overshooting [Fig. 3(b)]. The difference to the expected value at the longest switch-on time $\tilde{\tau}_n\Gamma = 100$ is less than 10^{-4} for the present improved approach. This significant improvement is also observed for the cumulative ($t = \infty > \tilde{\tau}_n$) error in $\text{Tr}[\rho^{i \rightarrow f}(\tilde{\tau}_n)]$. While this is at most $\sim 0.6\%$ in the previous approach, the present formalism yields a value of less than 0.01% in the whole range of switch-on times [see inset to Fig. 3(b)].

In general, then, the present formalism for multiple quenches results in an improved time evolution for observables, including an improved long time limit of observables and smaller discontinuities of observables after each quench. In the next section, we present and discuss the extension of this formalism to strictly infinite switch-on times.

IV. INFINITE SWITCH-ON TIME AND ACCURATE RESULTS IN THE LONG-TIME LIMIT

In this section, we extend the formalism in Sec. II to the infinite switch-on time limit and apply this to the long time limit of the spectral function and local thermodynamic observables in the interacting Anderson impurity model. We show that the resulting long time limit of the spectral function (Sec. IV A) and local thermodynamic observables (Sec. IV B) approach their expected values in the equilibrium final state to high accuracy. This conclusion is further supported by a (multiple quench) exact diagonalization study of the local level occupation number in the resonant level model (Sec. IV C).

The limit of an infinite switch-on time, $\tilde{\tau}_p \rightarrow +\infty$, can be implemented in Eq. (4) by applying the restriction that $r_1 = s_1$, ..., and $r_p = s_p$, resulting in

$$O(t \geq \tilde{\tau}_p \rightarrow \infty) = \sum_m \sum_{r_1 \dots r_p r_{p+1} s_{p+1}}^{\notin K_1 \dots K_p K_{p+1} K'_{p+1}} S_{r_{p+1} r_p}^m \dots S_{r_2 r_1}^m \rho_m^{i \rightarrow Q_1}(r_1, r_1) \times S_{r_1 r_2}^m \dots S_{r_p s_{p+1}}^m O_{s_{p+1} r_{p+1}}^m e^{-i(E_{r_{p+1}}^m - E_{s_{p+1}}^m)(t - \tilde{\tau}_p)}. \quad (8)$$

In the long time limit, infinitely long after the last quench, $O(t - \tilde{\tau}_n \rightarrow \infty)$ is calculated by applying the restriction that $r_{n+1} = s_{n+1}$ with $n = p$ to the above equation. Similarly, for the trace of the projected density matrix in the limit $\tilde{\tau}_p \rightarrow +\infty$, we have from Eq. (5)

$$I = \sum_m \sum_{r_1 \dots r_p r_{p+1}}^{\notin K_1 \dots K_p K_{p+1}} S_{r_{p+1} r_p}^m \dots S_{r_2 r_1}^m \rho_m^{i \rightarrow Q_1}(r_1, r_1) S_{r_1 r_2}^m \dots S_{r_p r_{p+1}}^m. \quad (9)$$

This equality is not satisfied exactly due to the use of the NRG approximation inherent in its derivation, but as demonstrated in Sec. III, the deviation of the trace from 1 is small. The small error is another reflection of the error in the long time limit of an observable within TDNRG.

A. Application to the long time limit of the spectral function

The general expression for the time-dependent local spectral function $A(\omega, t)$ of the Anderson impurity model for times after the pulse (i.e., for $t > \tilde{\tau}_n$) within the present multiple quench TDNRG approach is derived in Appendix A. We use this here in the limit $\tilde{\tau}_n \rightarrow \infty$ to discuss the long time limit of the spectral function $A(\omega) = A(\omega, t \rightarrow \infty)$.

Figures 4(a)-4(b) show $A(\omega)$ for a system that is gradually driven, (a), from an uncorrelated symmetric initial state to a correlated symmetric Kondo regime, and, (b), from a mixed valence regime to the symmetric Kondo regime. We use a logarithmic energy axis to focus attention on the long time limit of the low energy Kondo resonance at $|\omega| \lesssim T_K$. For both switching protocols, we show results for 1, 2, 8 and 32 quenches and also the results expected in the equilibrium final state and the single-quench result obtained by using the correlation self-energy Σ to improve the calculation of $A(\omega)$ ⁵⁸. In Fig. 4(a), the single quench result without the use of the correlation self-energy has a Kondo resonance which achieves only 60% of its Friedel sum rule value of 1 at $\omega = 0$ ⁵⁹, while the improvement in the single quench result upon using the correlation self-energy to calculate $A(\omega)$ is not sufficient to reduce the error in the Friedel sum rule to below 20%. In addition, the single quench TDNRG result for spectral functions suffer from additional substructures within the Kondo resonance at $|\omega| \lesssim T_K$, noticeable in Fig. 4(a), and discussed in detail elsewhere³⁸. On the other hand, a real improvement in the low energy Kondo resonance is observed within the multiple quench formalism upon increasing the number of quenches, with 8 quenches already yielding acceptable spectral functions with a less than 10% error in the Friedel sum rule and with 32 quenches yielding highly accurate results approaching the expected value of the spectral function in the equilibrium final state. The substructures are also absent for this number of quenches.

Similar conclusions also hold for the second type of switching shown in Fig. 4(b), in which the system is switched from the mixed valence to the symmetric Kondo regime. While signatures of the initial state particle-hole asymmetry in $A(\omega)$ are present in the final state spectral function for the 1, 2, and 8 quench results, this asymmetry is eliminated after 32 quenches, restoring the correct symmetry of the final state spectral function, which again also recovers accurately the expected equilibrium spectral function in the final state. In Appendix B we also consider the reverse of the quenches shown in Figs. 4(a)-4(b), i.e., from a correlated to an uncorrelated state and from a symmetric Kondo state to an asymmetric mixed valence regime. We find also for these quenches that the long time limit of the spectral function approaches the expected one in the equilibrium final state upon increasing the

number of quenches, with 32 quenches sufficing to obtain a similar accuracy as for the quenches in Figs. 4(a)-4(b).

Clearly, the quality of the TDNRG spectral functions at long times, a key input within the scattering states NRG^{31,32}, can be much improved by replacing the single quench TDNRG in Refs. 31 and 32 by the present multiple quench TDNRG. The use of the latter for this purpose should allow, in future, for an accurate study of nonequilibrium steady states for bias voltages on scales of order at least T_K . Furthermore, the high accuracy with which $Tr[\rho^{i \rightarrow f}(\tilde{\tau}_n)] = 1$ is satisfied in the present formalism (see inset to Fig. 3), guarantees that the spectral sum rule $\int d\omega A(\omega) = 1$ is satisfied to a correspondingly high accuracy.

B. Application to the long time limit of thermodynamic observables

For further insight into the multiple quench TDNRG results, we also look at the results for thermodynamic observables in the long time limit at finite temperatures. The percentage errors of the occupation number and the double occupancy in the long time limit when the system is switched from the asymmetric mixed valence regime to the symmetric Kondo regime are shown in Figs. 5(a) and 5(b), while the errors in the case of the reverse switching, i.e., from the symmetric Kondo regime to the asymmetric mixed valence regime, are shown in Figs. 5(c) and 5(d). The percentage error is defined by the relative difference between the expectation value of the local observable in the long time limit and the expected thermodynamic value in the final state, defined and denoted by $\delta O(t \rightarrow +\infty) = 100 \times \frac{O(t \rightarrow +\infty) - O_f}{O_f}$. In Fig. 5(a), the error of the occupation number in the case of a single quench is finite with an extremum at high temperature, and disappears only at the very highest temperature, $T > D$. With a larger number of quenches, 2 and 8, the absolute value of the error significantly decreases at low temperatures $T \leq T_K$, the extrema also decrease in magnitude and remain at around the same temperature as observed in the results for a single quench. In the case of 31 quenches, the error at low temperatures is closer to 0 than in the other cases, and the extremum is also smaller but still finite. In Fig. 5(b), the error of the double occupancy in the case of single quench is positive at low temperatures $T \lesssim T_K$ and negative at higher temperatures. With an increasing number of quenches, the magnitude of the error at $T \lesssim T_K$ is significantly reduced, approaching 0, while the error around the high temperature extremum changes less significantly, and converges to a finite value with increasing number of quenches. In the case of the reverse switching, Figs. 5(c) and 5(d), the side shoulders at temperatures in the range of $7T_K - 40T_K$ are also observed in addition to the extrema at higher temperature. With an increasing number of quenches, the errors decrease at low temperatures $T \leq T_K$, and the errors around the high-temperature peaks also decrease but still remain finite. The dependence of the error in the trace of the projected density matrices on the logarithmic discretization parameter Λ is discussed in Appendix D. The main finding there is that the error decreases with increasing Λ for a

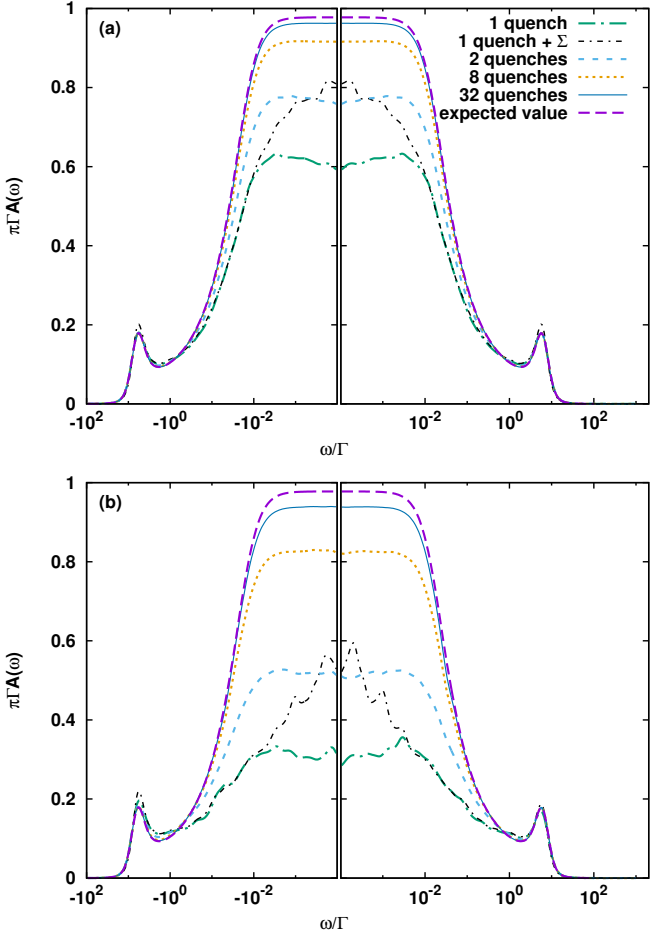


FIG. 4. Normalized spectral function ($\pi\Gamma A(\omega)$) vs normalized frequency ω/Γ in the long-time limit and infinite switch-on time for 2, 8 and 32 quenches compared to that from the single-quench TDNRG with (1 quench + Σ) and without (1 quench) the use of the self-energy⁵⁸. Also shown is the expected value of the spectral function in the equilibrium final state. (a): for switching from the noninteracting with $\epsilon_d^i = U^i = 0$ to the interacting system with $\epsilon_d^f = -U^f/2$, $U^f = 12\Gamma$. (b): for switching from the asymmetric mixed valence regime with $\epsilon_d^i = 0$ and $U^i = 12\Gamma$ to the symmetric Kondo regime with $\epsilon_d^f = -U^f/2$, $U^f = 12\Gamma$. $\Gamma = 10^{-3}D$, and $D = 1$ is the half-bandwidth. Calculations were for essentially zero temperature $T = 10^{-4}T_K$, with T_K the Kondo temperature in the final state, NRG parameters: $\Lambda = 4$, $E_{\text{cut}} = 24$, and $N_z = 8$ values for the z-averaging.

sufficiently large number of quenches.

As mentioned in our previous paper³⁵, the error in the long time limit does not only depend on the size of the quench but also on the largest incoherent excitation of the final state, $\epsilon_{\text{inc}}^{\text{max}} = \max(|\epsilon_f|, |\epsilon_f + U_f|, \Gamma)$. Apparently, the TDNRG calculation for multiple quenches may overcome the first problem of quench size by dividing it into a sequence of smaller ones, but not the second problem since $\epsilon_{\text{inc}}^{\text{max}}$ is the same in both calculations for single quench and multiple quenches. It suggests that the observed extrema at finite temperature may originate from the incoherent excitations.

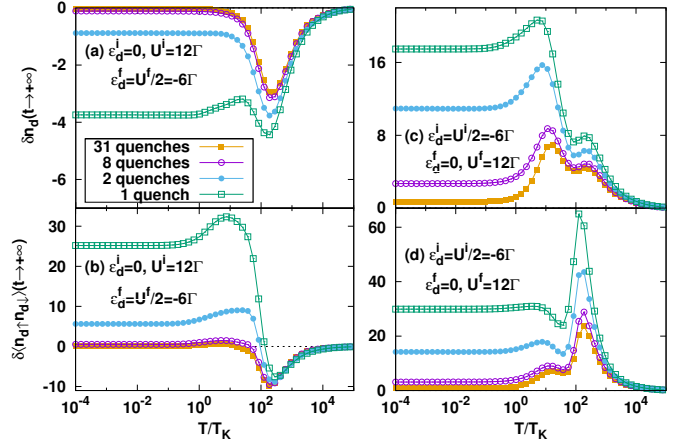


FIG. 5. The percentage error in the expectation value of local observables in the long-time limit vs rescaled temperature T/T_K after a switch from the asymmetric mixed valence to symmetric Kondo regime, (a) and (b), and a switch from the symmetric Kondo regime to the asymmetric mixed valence regime, (c) and (d), with initial and final state parameters shown in the legends. The system is switched by applying 1, 2, 8 or 31 quenches on the local level and/or local Coulomb term, either, only on ϵ_d in (a) and (b), or, on both ϵ_d and U in (c) and (d). (a) and (c) show the errors of the occupation numbers in the long time limit, (b) and (d) show the errors in the double occupancy. T_K is the Kondo temperature of the symmetric system, $\Gamma = 10^{-3}D$, and $D = 1$ is the half-bandwidth. The calculations are for $\Lambda = 4.0$, $E_{\text{cut}} = 24$, and $N_z = 4$ values were used for the z-averaging.

These results suggest that the TDNRG calculation for multiple quenches systematically improves the long time limit of observables in the low temperature regime $T \leq T_K$, but not in the high temperature regime for temperatures of order the scale of the highest energy incoherent excitation. Nevertheless, the TDNRG presented is promising for the study of the Kondo effect out of equilibrium, where the interest is primarily on low temperatures where a Kondo effect is present, and on the observed destruction of the Kondo resonance when the bias voltage is increased to values comparable to and above T_K .

C. TDNRG vs Exact diagonalization

Finally, we apply the TDNRG formalism for multiple quenches with infinite switch-on time to the resonant level model, i.e., the Anderson impurity model with $U = 0$, and compare the results to those of the exact diagonalization (ED) study.

In the ED calculations, the conduction band is also discretized logarithmically using the parameter Λ as in the NRG calculations, and the resulting model is likewise mapped onto an impurity coupled to a semi-infinite chain. The ED is applied to finite size initial and final state Hamiltonians of length N , corresponding to the longest chain diagonalized within a TDNRG approach⁶⁰, and one can then determine from the resulting single particle levels and eigenstates the time evolution

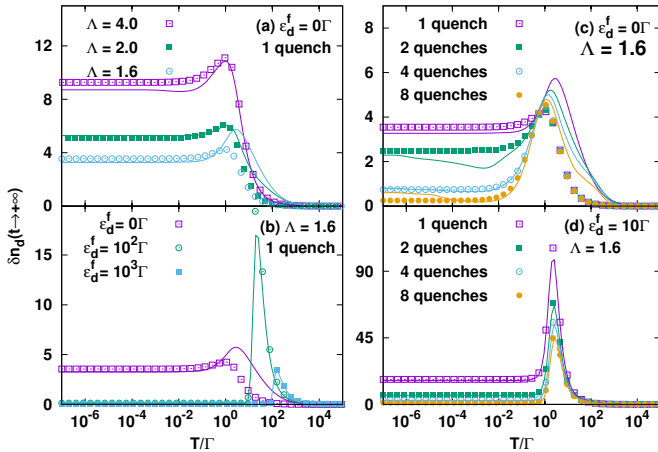


FIG. 6. The percentage error in the expectation value of the occupation number in the long-time limit vs temperature calculated by TDNRG (solid lines) and the exact diagonalization (symbols) applied to the resonant level model. a), the calculations for single quench are with a fixed final state level position $\varepsilon_d^f = 0$, a fixed quench size, $\Delta\varepsilon_d = \varepsilon_d^f - \varepsilon_d^i = 6\Gamma$, and for different values of Λ . b), the calculations are with a fixed Λ and fixed quench size $\Delta\varepsilon_d = 6\Gamma$, and different values of ε_d^f . The calculations for multiple quenches with fixed quench size $\Delta\varepsilon_d$ and fixed Λ , with $\varepsilon_d^f = 0\Gamma$ in (c) and with $\varepsilon_d^f = 10\Gamma$ in (d). NRG parameters: the number of kept states in each iteration $N_s = 900$, and $N_z = 8$ values for the z-averaging.

of observables following a quench. We have generalized the formulae for the time evolution of observables within this approach, to the case of multiple quenches, and for more details we refer the reader to Appendix E. In the ED calculation, there is no truncation of states as in the NRG calculation, and one can therefore obtain approximation-free results (no NRG approximation enters). The method can not be applied to the Anderson impurity model with $U \neq 0$, however. Since it also solves the same discrete model as in TDNRG, it can be used as a benchmark to check the TDNRG calculations^{34,60}. In addition, it can be formulated for infinite switch-on times (Appendix E); this allows us to verify that an infinite switch-on time improves the long-time limit of thermodynamic observables, as in the present multiple quench TDNRG approach.

In Fig. 6, we show the percentage error of the occupation number in the long time limit calculated by both TDNRG and ED. Clearly, the TDNRG results almost overlap with the ED results. The difference is primarily visible at high temperatures and originates from the use of the truncation in the TDNRG (and absent in ED). The ED calculation for a single quench in Figs. 6(a) and 6(b) exhibits the same problem as in the TDNRG calculation, i.e., even at low temperature, where both methods yield largely the same result, this long time result exhibits a finite “error”. More precisely, this is largely not an error as such, but represents a deviation from the expected value for a continuum bath due to the use of a logarithmically discretized bath. The latter is known to prevent perfect thermalization of observables to their expected values at long times within the single-quench TDNRG approach^{34,38,40}.

The percentage error, at low temperature, is thus finite in both methods at low temperature and it shows an extremum at high temperature in both methods. Any remaining difference between the TDNRG and ED results can be attributed to truncation errors in the TDNRG approach (which can be seen to be small). Thus, the logarithmically discretized bath, and the consequent imperfect thermalization, is the main source of “error” in the long time limit of observables. Arguably this imperfect thermalization should not be termed an “error” of the single-quench TDNRG approach, but a feature of this approach. With decreasing Λ in Fig. 6 (a), i.e., better approximating the continuum bath, the error decreases significantly, and the extremum is still located at around the same high temperature. By changing ε_d^f in Fig. 6 (b), we can determine the relationship between the extremum at high temperature and the incoherent excitations, as defined above in Sec. IV B. For example, when $\varepsilon_d^f = 0\Gamma$, then $\varepsilon_{inc}^{max} = \Gamma$, we have that the corresponding extremum appears exactly at $T = \Gamma$. With larger ε_d^f , we have $\varepsilon_{inc}^{max} = \varepsilon_d^f$, and the extremum appears at higher temperatures around ε_d^f , but not exactly, due to the interference with the lower energy scale Γ .

Turning now to the TDNRG and ED results for multiple quenches, we show in Figs. 6(c) and 6(d) the percentage error in the long time limit of the occupation number for two equal sized quenches with two different values of ε_d^f and in the limit of an infinite switch-on time. With increasing number of quenches, the errors in both cases are reduced close to 0 at low temperature but the errors around the high temperature extremum at $T \approx \varepsilon_{inc}^{max} = \varepsilon_d^f$ are always finite. In Fig. 6 (c), ε_{inc}^{max} equals the lowest energy scale of the final system, then the extrema in the results with different number of quenches are almost the same.

In summary, the ED calculations for both single and multiple quenches without any approximation also show errors in the occupation numbers in the long time limit, with extrema at high temperatures as in TDNRG. These are largely due to the imperfect thermalization in the long time limit due to the use of a logarithmically discretized bath. Dividing a large quench into a sequence of smaller ones with an infinite switch-on time, implemented in the ED calculations presented here, also improves the long time limit of observables at low temperatures as in TDNRG. Any remaining small difference between the ED and TDNRG results is due the use of truncation in the latter (absent in the former). This further supports the precision of the multiple quench TDNRG results presented here for infinite switch-on times.

V. CONCLUSIONS

In this paper, we developed an alternative multiple quench TDNRG formalism for general pulses, which reduces further the effect of the NRG approximation on the time evolution of observables. We showed this by comparison with the previous approach^{35,36}. Specifically, the trace of the projected density matrix versus time remains closer to 1 and the discontinuities in the time evolution of observables following quenches

are significantly reduced. Both approaches improve the long time limit of observables for increasing switch-on times, i.e., with increasing adiabaticity of the switching from initial to final state. However, the present approach shows a monotonic and faster convergence of the long time limit with increasing switch-on time than the previous approach. Moreover, the present formalism allows the limit of infinite switch-on time to be straightforwardly taken analytically, which is impossible in the previous formalism.

We also formulated the spectral function within the new formalism, both for finite and infinite switch-on times. For infinite switch-on time, we showed that the long time limit of the zero temperature spectral function approached its value in the equilibrium final state with high accuracy: the Friedel sum rule was satisfied to within a few %, which is to be compared with the much larger error of order typically 15% in the single quench approach^{32,38}. Additional features, at $|\omega| \lesssim T_K$, found in the single quench approach³⁸, are absent in the present approach. Hence, the present approach yields accurate results for the long time limit of spectral functions for systems switched between an arbitrary initial and an arbitrary final state, overcoming the problems encountered within the single

quench approach^{38,40}. This improvement is particularly important for an accurate description of nonequilibrium steady states of quantum impurity systems, since methods such as the scattering states NRG approach³¹ for addressing steady states, rely on an accurate time evolved spectral function in the long time limit. In future, we therefore plan to use the present multiple quench formalism to address nonequilibrium steady states in quantum impurity systems and to compare with known exact results⁴⁸ and other approaches^{20,31,51}.

ACKNOWLEDGMENTS

H. T. M. Nghiem acknowledges the support by Vietnam National Foundation for Science and Technology Development (NAFOSTED) under grant number 103.2-2017.353. We acknowledge support by the Deutsche Forschungsgemeinschaft via the “Research Training Group 1995” and supercomputer support by the John von Neumann institute for Computing (Jülich).

Appendix A: Spectral function in the long time limit

In order to evaluate the spectral function, we require an expression for the retarded two-time Green function $G_{BC}(t + t', t) = -i\theta(t') \text{Tr}\{\hat{\rho}[\hat{B}(t + t'), \hat{C}(t)]_s\}$ within TDNRG. We work within the complete basis set and full density matrix approach^{53,61,62}. Since we are here only interested in the long-time limit after the last quench, $t + t' > t > \tilde{\tau}_n$, we can write

$$\begin{aligned} G_{BC}(t + t', t) &= -i\theta(t') \text{Tr}\{\hat{\rho}[\hat{B}(t + t'), \hat{C}(t)]_s\} \\ &= -i\theta(t') \text{Tr}\{\hat{\rho}[e^{iH^f(t+t'-\tilde{\tau}_n)} \dots e^{iH^{Q_1}\tau_1} \hat{B} e^{-iH^{Q_1}\tau_1} \dots e^{-iH^f(t+\tau_n)}, e^{iH^f(t-\tilde{\tau}_n)} \dots e^{iH^{Q_1}\tau_1} \hat{C} e^{-iH^{Q_1}\tau_1} \dots e^{-iH^f(t-\tilde{\tau}_n)}]_s\} \\ &= -i\theta(t') \text{Tr}\{e^{-iH^f(t-\tilde{\tau}_n)} \dots e^{-iH^{Q_1}\tau_1} \hat{\rho} e^{iH^{Q_1}\tau_1} \dots e^{iH_f(t-\tilde{\tau}_n)} [e^{iH^f t'} \hat{B} e^{-iH^f t'}, \hat{C}]_s\} \end{aligned} \quad (\text{A1})$$

Inserting decompositions of unity $1 = \sum_{lem} |lem\rangle\langle lem|$ in the above gives,

$$\begin{aligned} G_{BC}(t + t', t) &= -i\theta(t') \sum_{\substack{lem \\ l'e'm' \\ l'e'm'' \\ l'e'm''}} \sum_{\substack{l_1e_1m_1 \\ l'_1e'_1m'_1 \\ l'_1e'_1m'_1 \\ l'_1e'_1m'_1}} \dots \sum_{\substack{l_ne_nm_n \\ l'_ne'_nm'_n \\ l'_ne'_nm'_n \\ l'_ne'_nm'_n}} {}_f\langle lem| e^{-iH^f(t-\tilde{\tau}_n)} e^{-iH^{Q_n}\tau_n} |l_ne_nm_n\rangle_{Q_n} \dots {}_{Q_2}\langle l_2e_2m_2| e^{-iH^{Q_1}\tau_1} |l_1e_1m_1\rangle_{Q_1} \\ &\quad \times {}_{Q_1}\langle l_1e_1m_1| \hat{\rho} |l'_1e'_1m'_1\rangle_{Q_1} {}_{Q_1}\langle l'_1e'_1m'_1| e^{iH^{Q_1}\tau_1} |l'_2e'_2m'_2\rangle_{Q_2} \dots {}_{Q_n}\langle l'_ne'_nm'_n| e^{iH^{Q_n}\tau_n} e^{iH_f(t-\tilde{\tau}_n)} |l'e'm'\rangle_f \\ &\quad \times {}_f\langle l'e'm'| e^{iH^f t'} \hat{B} e^{-iH^f t'} |l'e'm'\rangle_{ff} {}_f\langle l'e'm'| \hat{C} |l'e'm'\rangle_{ff} {}_f\langle l'e'm'| e^{iH^f t'} \hat{B} e^{-iH^f t'} |l'e'm'\rangle_f \end{aligned} \quad (\text{A2})$$

Converting the multiple-shell summations over discarded states into a shell-diagonal restricted sum⁵⁶ leads to

$$\begin{aligned} G_{BC}(t + t', t) &= -i\theta(t') \sum_m \sum_{rsqr_1s_1 \dots r_ns_n} {}_{\#KK'K''K_1K'_1 \dots K_nK'_n} S_{rr_n}^m \dots S_{r_2r_1}^m \rho_m^{i \rightarrow Q_1}(r_1, s_1) e^{-i(E_{r_1}^m - E_{s_1}^m)\tau_1} S_{s_1s_2}^m \dots e^{-i(E_{r_n}^m - E_{s_n}^m)\tau_n} S_{s_ns}^m e^{-i(E_r^m - E_s^m)(t - \tilde{\tau}_n)} \\ &\quad \times (B_{sq}^m e^{i(E_s^m - E_q^m)t'} C_{qr}^m + C_{sq}^m B_{qr}^m e^{i(E_q^m - E_r^m)t'}). \end{aligned} \quad (\text{A3})$$

Fourier transforming this Green function with respect to the time difference t' results in

$$\begin{aligned} G_{BC}(\omega, t) &= \sum_m \sum_{rsqr_1s_1 \dots r_ns_n} {}_{\#KK'K''K_1K'_1 \dots K_nK'_n} S_{rr_n}^m \dots S_{r_2r_1}^m \rho_m^{i \rightarrow Q_1}(r_1, s_1) e^{-i(E_{r_1}^m - E_{s_1}^m)\tau_1} S_{s_1s_2}^m \dots e^{-i(E_{r_n}^m - E_{s_n}^m)\tau_n} S_{s_ns}^m e^{-i(E_r^m - E_s^m)(t - \tilde{\tau}_n)} \\ &\quad \times \left(\frac{B_{sq}^m C_{qr}^m}{\omega + E_s^m - E_q^m + i\eta} + \frac{C_{sq}^m B_{qr}^m}{\omega + E_q^m - E_r^m + i\eta} \right). \end{aligned} \quad (\text{A4})$$

Then we have the spectral function, $A(\omega, t) = -Im[G(\omega, t)]/\pi$, at the long time limit $t - \tilde{\tau}_n \rightarrow +\infty$ with finite $\tau_{p=1,\dots,n}$

$$A(\omega, t) = \sum_m \sum_{rqr_1s_1\dots r_ns_n}^{\notin KK'K_1K'_1\dots K_nK'_n} S_{rr_n}^m \dots S_{r_2r_1}^m \rho_m^{i \rightarrow Q_1}(r_1, s_1) e^{-i(E_{r_1}^m - E_{s_1}^m)\tau_1} S_{s_1s_2}^m \dots e^{-i(E_{r_n}^m - E_{s_n}^m)\tau_n} S_{s_ns_n}^m \times [B_{rq}^m C_{qr}^m \delta(\omega + E_r^m - E_q^m) + C_{sq}^m B_{qr}^m \delta(\omega + E_q^m - E_r^m)], \quad (\text{A5})$$

and the long time limit with $\tau_{p=1,\dots,n} \rightarrow +\infty$

$$A(\omega, t) = \sum_m \sum_{rqr_1\dots r_n}^{\notin KK'K_1\dots K_n} S_{rr_n}^m \dots S_{r_2r_1}^m \rho_m^{i \rightarrow Q_1}(r_1, r_1) S_{r_1r_2}^m \dots S_{r_nr_n}^m [B_{rq}^m C_{qr}^m \delta(\omega + E_r^m - E_q^m) + C_{sq}^m B_{qr}^m \delta(\omega + E_q^m - E_r^m)]. \quad (\text{A6})$$

Appendix B: Spectral function in the long time limit: reverse quenches

We show in Figs. 7(a)-7(b) the long time limit of the spectral function $A(\omega) = A(\omega, t \rightarrow \infty)$ for 1, 2, 8 and 32 quenches for the reverse of the two quenches in Figs. 4(a)-4(b). While $A(\omega)$ exhibits significant substructures at low energies for a small number of quenches, these substructures are rapidly suppressed upon increasing the number of quenches. For 32 quenches, we recover in both cases the expected equilibrium spectral function of the final state to high accuracy. Thus, the Friedel sum rule in Fig. 7(a) is recovered to within 5%, while for the quench into the mixed valence regime in Fig. 7(b) it is recovered to within 3%. In the latter, the mixed valence resonance is correctly renormalized upwards from its bare value at $\omega = \varepsilon_d^f = 0$ to $\omega = \tilde{\varepsilon}_d^f \approx \Gamma$ by the Coulomb interaction, while the higher lying satellite peak is also correctly located at $\omega \approx \varepsilon_d^f + U^f \approx 12\Gamma$ ⁶³. Similarly, for the quench in Fig. 7(a) we see that $A(\omega)$ for 32 quenches recovers the noninteracting resonant level of the final state with halfwidth at half maximum given by Γ and centered at zero energy. In conclusion, for a sufficient number of quenches, the present formalism for an infinite switch-on time is able to describe the long time limit of the spectral function to high accuracy. In the next section, we discuss the effects of a finite switch-on time on $A(\omega)$ in the long-time limit.

Appendix C: Spectral function in the long time limit: dependence on a finite switch-on time

We show in Fig. 8 the dependence of the long time limit of the spectral function $A(\omega) = A(\omega, t \rightarrow \infty)$ on the switch-on time $\tau = \tilde{\tau}_n$. As with the occupation number, the long time limit of the spectral function also improves and approaches the expected value in the equilibrium final state with increasing switch-on time τ . In the case of switching from the asymmetric to symmetric Kondo regime, Fig. 8(b), the spectral function in the long time limit becomes more symmetric with increasing τ . However, the spectral function shows small additional structures at $|\omega| < T_K$ even when the switch-on time τ exceeds the time scale $1/T_K$ for the formation of the Kondo resonance^{38,64}. The error in the spectral sum rule

$\int_{-\infty}^{+\infty} d\omega A(\omega, t \rightarrow \infty) = 1$ is violated in this case by 0.1%. This is attributed to the NRG approximation in the multiple quench formalism, which results in a cumulative error in the trace of the projected density matrix and a discontinuity in the time evolution of observables, as discussed in Sec. III. In the case of switching from a noninteracting to an interacting system, Fig. 8(a), the long time limit of the spectral function lies closer to the expected result than that for the second switching protocol in Fig. 8 (b) for each τ . However, at the longest τ , additional structures within the Kondo resonance at $|\omega| < T_K$ are still visible, attributable to the more pronounced effect of the NRG approximation in the case of finite switch-on times. The above findings support the conclusion that accurate results can be obtained for the long time limit of the spectral function within TDNRG by replacing a single large quench by a sequence of smaller quenches and switching the system slowly from one state to the other (i.e., with increasing τ). The most accurate results are obtained in the limit of a large number of quenches and for $\tau \rightarrow \infty$ as supported by the results in Sec. IV A and Appendix B.

Appendix D: Calculations with different Λ

We show in Fig. 9 the errors of the traces of the projected density matrices versus temperature for calculations with different Λ . In the calculations with $\Lambda = 1.6$ in Fig. 9(a) and Fig. 9(c), the percentage errors are as large as approximately 3% at low temperatures, and they exhibit an extremum of up to approximately 6% at high temperatures. The absolute values of the errors are non-monotonic with respect to the number of quenches. For the case of 31 quenches, the errors in both quenches are similar, suggesting that for the large number of quenches the error strongly depends on the quench size. The calculations with $\Lambda = 4$, Fig. 9(b) and Fig. 9(d), result in much smaller errors than for $\Lambda = 1.6$. Except for the error in the case of 2 quenches in Fig. 9 (b) which is up to around 1.5%, all the errors for a larger number of quenches are less than 0.6%. We conclude that the formalism presented here results in smaller errors in the trace of the projected density matrices with increasing values of Λ .

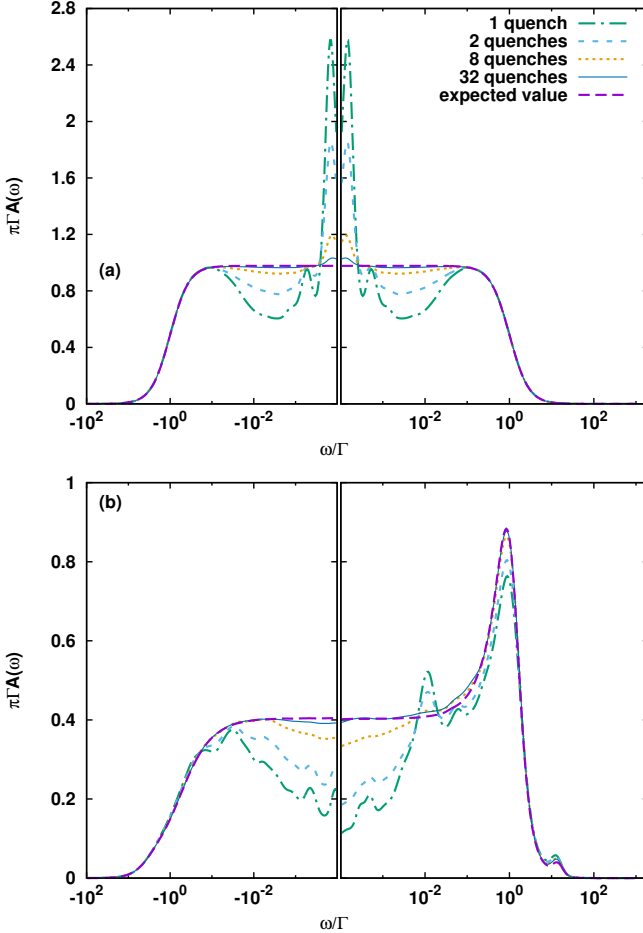


FIG. 7. Normalized spectral function ($\pi\Gamma A(\omega)$) vs normalized frequency ω/Γ in the long-time limit and infinite switch-on time for 2, 8 and 32 quenches compared to that from the single-quench TD-NRG. Also shown is the expected value of the spectral function in the equilibrium final state. (a) Switching from an interacting system with $\varepsilon_d^i = -U^i/2$, $U^i = 12\Gamma$ to a noninteracting system with $\varepsilon_d^f = U^f = 0$. (b) Switching from a system in the symmetric Kondo regime with $\varepsilon_d^i = -U^i/2$, $U^i = 12\Gamma$ to one in the asymmetric mixed valence regime with $\varepsilon_d^f = 0$ and $U^f = 12\Gamma$. $\Gamma = 10^{-3}D$, and $D = 1$ is the half-bandwidth. Calculations were for essentially zero temperature $T = 10^{-4}T_K$, with T_K the Kondo temperature in the initial state, NRG parameters: $\Lambda = 4$, $E_{\text{cut}} = 24$, and $N_z = 8$ values for the z-averaging.

Appendix E: Exact diagonalization of the resonant level model with multiple quenches

The real-time evolution of a system, modeled by the resonant level model (RLM), following a single quench can be calculated via exact diagonalization (ED)⁶⁰. In this appendix, we derive results for the time dependence of the occupation number of the resonant level model, $\langle n_d(t) \rangle$, and also for the time dependence of the conduction electron orbital occupation numbers, first for the case of two quenches, and then generalizing this to the case of an arbitrary number of quenches. The presented expressions are then free of any approxima-

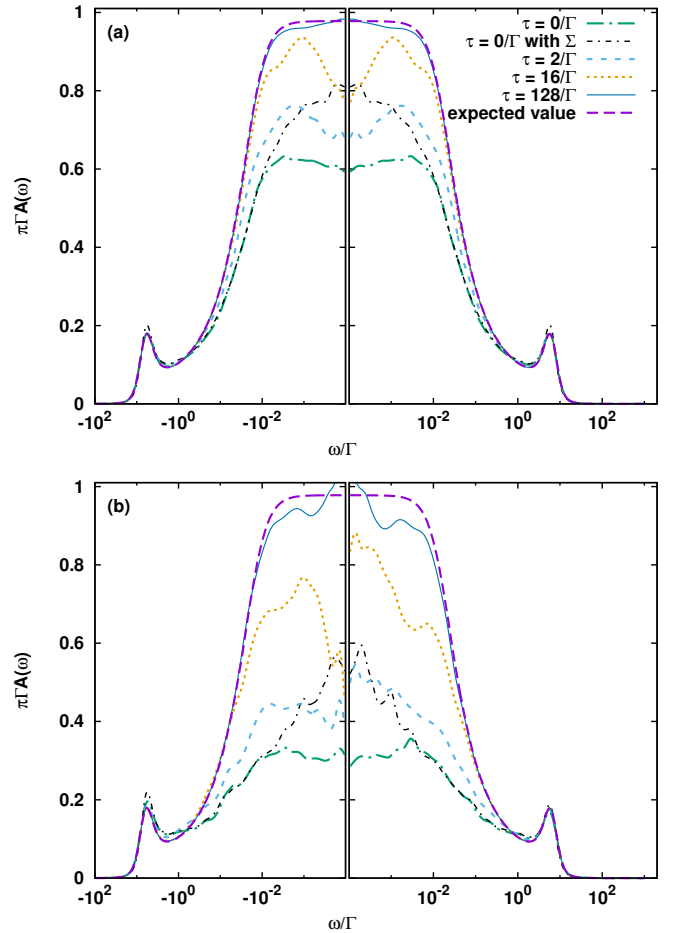


FIG. 8. Spectral function in the long-time limit $A(\omega, t \rightarrow \infty)$ vs ω/Γ for different finite switch-on times $\tau = \tau_n$. Also shown is the expected equilibrium spectral function in the final state. (a) Switching from a noninteracting regime with $\varepsilon_d^i = 0$ and $U^i = 0$ to an interacting Kondo regime with $\varepsilon_d^f = -U^f/2$ and $U^f = 12\Gamma$. (b) Switching from the asymmetric mixed valence regime with $\varepsilon_d^i = 0$ and $U^i = 12\Gamma$ to the symmetric Kondo regime with $\varepsilon_d^f = -U^f/2$ and $U^f = 12\Gamma$. $\Gamma = 10^{-3}D$, with $D = 1$ the half-bandwidth. Calculations were for essentially zero temperature, $T = 10^{-4}T_K$, with T_K the Kondo temperature in the initial state. NRG parameters: $\Lambda = 4$, $E_{\text{cut}} = 24$, and $N_z = 8$ values for the z-averaging.

tions, both for finite and infinite switch-on times.

In the ED of the RLM, the conduction band is also discretized with the parameter Λ and mapped onto a Wilson chain as in the NRG calculation. Then we have the following discrete model,

$$\begin{aligned}
 H_N(t) &= \varepsilon_d(t)d^\dagger d + V(t)(d^\dagger c_0 + c_0^\dagger d) + \sum_{n=0}^{N-2} t_n(c_n^\dagger c_{n+1} + c_{n+1}^\dagger c_n) \\
 &= \vec{a}^\dagger M(t) \vec{a},
 \end{aligned} \tag{E1}$$

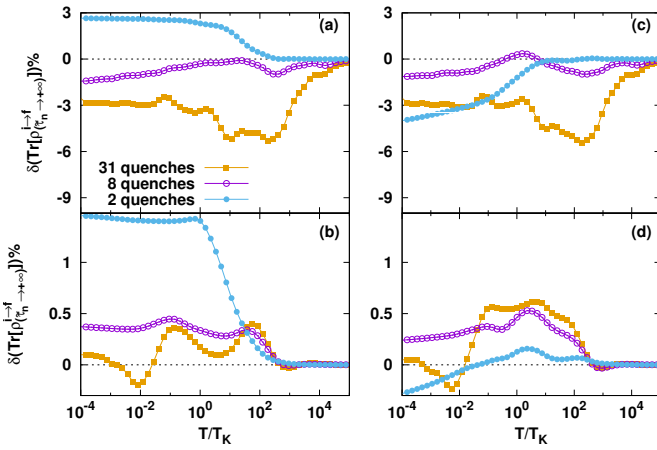


FIG. 9. Percentage deviation of the trace of the projected density matrix away from 1 for different Λ vs rescaled temperature T/T_K . Upper panels (a) and (c) are for $\Lambda = 1.6$. Lower panels (b) and (d) are for $\Lambda = 4$. Left panels (a) and (b) were for switching from the asymmetric mixed valence regime with $\epsilon_d^i = 0$ and $U^i = 12\Gamma$ to the symmetric Kondo regime with $\epsilon_d^f = -U^f/2$ and $U^f = 12\Gamma$, while, right panels (c) and (d) were for switching from the symmetric Kondo regime with $\epsilon_d^i = -U^i/2$ and $U^i = 12\Gamma$ to the asymmetric mixed valence regime with $\epsilon_d^f = 0$ and $U^f = 12\Gamma$. $\Gamma = 10^{-3}D$, with $D = 1$ the half-bandwidth. T_K the Kondo temperature of the symmetric Kondo state. NRG parameters for the calculations with $\Lambda = 1.6$: $N_z = 8$ and the number of kept states $N_s = 900$. For the calculations with $\Lambda = 4$, the parameters are the same to those in Fig. 5.

with $\vec{a} = \begin{pmatrix} d \\ c_0 \\ \vdots \end{pmatrix}$, $\vec{a}^\dagger = (d^\dagger \ c_0^\dagger \ \cdots)$, and

$$M(t) = \begin{pmatrix} \epsilon_d(t) & V & 0 & 0 \\ V & 0 & t_0 & 0 \\ 0 & t_0 & 0 & \ddots \\ 0 & 0 & \ddots & \ddots \end{pmatrix}. \quad (\text{E2})$$

$M(t)$ can be diagonalized as follows

$$M(t) = U(t)^\dagger \text{diag}(\epsilon_1(t), \epsilon_2(t), \dots) U(t). \quad (\text{E3})$$

$H(t)$ is represented in Fig. 10, in which each Hamiltonian

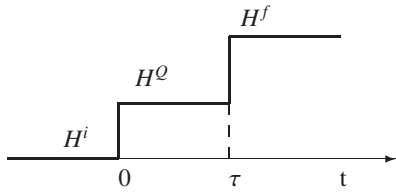


FIG. 10. A system driven from the initial H^i to the final state H^f via the intermediate state described by $\{H^Q\}$.

can be expressed in the diagonal form as $H^i = \sum_n \epsilon_n^i f_n^{i\dagger} f_n^i$,

$$H^Q = \sum_n \epsilon_n^Q f_n^{Q\dagger} f_n^Q, \text{ and } H^f = \sum_n \epsilon_n^f f_n^{f\dagger} f_n^f \text{ with}$$

$$f_n^i = \sum_l U_{nl}^i \alpha_l, \quad f_n^Q = \sum_l U_{nl}^Q \alpha_l, \quad f_n^f = \sum_l U_{nl}^f \alpha_l \quad (\text{E4})$$

$$f_n^{i\dagger} = \sum_l \alpha_l^\dagger U_{nl}^{i\dagger}, \quad f_n^{Q\dagger} = \sum_l \alpha_l^\dagger U_{nl}^{Q\dagger}, \quad f_n^{f\dagger} = \sum_l \alpha_l^\dagger U_{nl}^{f\dagger}. \quad (\text{E5})$$

The operator for the occupation number of site m is defined as

$$n_m = \alpha_m^\dagger \alpha_m = \begin{cases} d^\dagger d & m = 0; \\ c_{m-1}^\dagger c_{m-1} & m > 1. \end{cases} \quad (\text{E6})$$

The expectation value of the occupation number is given by

$$\langle n_m(t > \tau) \rangle = \text{Tr}[\rho(t) n_m], \quad (\text{E7})$$

with $\rho(t) = e^{-iH^f(t-\tau)} e^{-iH^Q\tau} \rho_0 e^{iH^Q\tau} e^{iH^f(t-\tau)}$ and $\rho_0 = \frac{e^{-\beta H^i}}{Z} = \frac{e^{-\beta \sum_n \epsilon_n^i f_n^{i\dagger} f_n^i}}{\text{Tr}[e^{-\beta \sum_n \epsilon_n^i f_n^{i\dagger} f_n^i}]}.$ Then we have

$$\begin{aligned} \langle n_m(t > \tau) \rangle &= \text{Tr}[e^{-iH^f(t-\tau)} e^{-iH^Q\tau} \rho_0 e^{iH^Q\tau} e^{iH^f(t-\tau)} n_m] \\ &= \text{Tr}[e^{-iH^Q\tau} \rho_0 e^{iH^Q\tau} \underbrace{e^{iH^f(t-\tau)} n_m e^{-iH^f(t-\tau)}}_{n_m(t-\tau)}]. \end{aligned} \quad (\text{E8})$$

$$\begin{aligned} n_m(t-\tau) &= e^{iH^f(t-\tau)} \underbrace{\alpha_m^\dagger \alpha_m}_{n_m} e^{-iH^f(t-\tau)} \\ &= \sum_{nn'} e^{iH^f(t-\tau)} f_n^{f\dagger} f_{n'}^f e^{-iH^f(t-\tau)} U_{nm}^f U_{mn'}^{f\dagger} \\ &= \sum_{nn'} \underbrace{e^{iH^f(t-\tau)} f_n^{f\dagger} e^{-iH^f(t-\tau)}}_{f_n^{f\dagger}(t-\tau)} \underbrace{e^{iH^f(t-\tau)} f_{n'}^f e^{-iH^f(t-\tau)}}_{f_{n'}^f(t-\tau)} U_{nm}^f U_{mn'}^{f\dagger} \\ &= \sum_{nn'} e^{i(\epsilon_n^f - \epsilon_{n'}^f)(t-\tau)} f_n^{f\dagger} f_{n'}^f U_{nm}^f U_{mn'}^{f\dagger}, \end{aligned} \quad (\text{E9})$$

since $\partial_{(t-\tau)} f_n^f(t-\tau) = i[H^f, f_n^f(t-\tau)] = -i\epsilon_n^f f_n^f(t-\tau)$, then $f_n^f(t-\tau) = e^{-i\epsilon_n^f(t-\tau)} f_n^f$. Substituting E9 into E8, we have

$$\begin{aligned} \langle n_m(t > \tau) \rangle &= \sum_{nn'} e^{i(\epsilon_n^f - \epsilon_{n'}^f)(t-\tau)} \text{Tr}[e^{-iH^Q\tau} \rho_0 e^{iH^Q\tau} f_n^{Q\dagger} f_n^Q] U_{nm}^f U_{mn'}^{f\dagger} \\ &= \sum_{nn'} e^{i(\epsilon_n^f - \epsilon_{n'}^f)(t-\tau)} \sum_{kk'} \text{Tr}[e^{-iH^Q\tau} \rho_0 e^{iH^Q\tau} f_k^{Q\dagger} f_k^Q] \\ &\quad \times (U^Q U^{f\dagger})_{kn} (U^f U^{Q\dagger})_{n'k'} U_{nm}^f U_{mn'}^{f\dagger}. \end{aligned} \quad (\text{E10})$$

Similarly, the trace in E10 is evaluated as follows

$$\begin{aligned} &\text{Tr}[e^{-iH^Q\tau} \rho_0 e^{iH^Q\tau} f_k^{Q\dagger} f_k^Q] \\ &= \text{Tr}[\rho_0 e^{iH^Q\tau} f_k^{Q\dagger} e^{-iH^Q\tau} e^{iH^Q\tau} f_{k'}^Q e^{-iH^Q\tau}] \\ &= e^{i(\epsilon_k^Q - \epsilon_{k'}^Q)\tau} \text{Tr}[\rho_0 f_k^{Q\dagger} f_{k'}^Q] \\ &= e^{i(\epsilon_k^Q - \epsilon_{k'}^Q)\tau} \sum_{qq'} \underbrace{\text{Tr}[\rho_0 f_q^{i\dagger} f_{q'}^i] (U^i U^{Q\dagger})_{qk} (U^Q U^{i\dagger})_{k'q'}}_{f(\epsilon_q^i) \delta_{qq'}} \\ &= e^{i(\epsilon_k^Q - \epsilon_{k'}^Q)\tau} \sum_q f(\epsilon_q^i) (U^i U^{Q\dagger})_{qk} (U^Q U^{i\dagger})_{k'q}, \end{aligned} \quad (\text{E11})$$

in which $f(\epsilon_q^i)$ is the Fermi-Dirac distribution. Substituting E11 into E10, we have

$$\begin{aligned} \langle n_m(t > \tau) \rangle &= \sum_{nn'} e^{i(\epsilon_n^f - \epsilon_{n'}^f)(t-\tau)} \sum_{kk'} e^{i(\epsilon_k^Q - \epsilon_{k'}^Q)\tau} \sum_q f(\epsilon_q^i) (U^i U^{Q\dagger})_{qk} (U^Q U^{i\dagger})_{k'q} \\ &\quad \times (U^Q U^{f\dagger})_{kn} (U^f U^{Q\dagger})_{n'k'} U_{nn'}^f U_{mn'}^{f\dagger}. \end{aligned} \quad (\text{E12})$$

Defining

$$n_{kk'}^{i \rightarrow Q} = \sum_q f(\epsilon_q^i) (U^i U^{Q\dagger})_{qk} (U^Q U^{i\dagger})_{k'q} \quad (\text{E13})$$

$$n_{nn'}^{i \rightarrow f} = \sum_{kk'} e^{i(\epsilon_k^Q - \epsilon_{k'}^Q)\tau} n_{kk'}^{i \rightarrow Q} (U^Q U^{f\dagger})_{kn} (U^f U^{Q\dagger})_{n'k'}, \quad (\text{E14})$$

we have

$$\langle n_m(t > \tau) \rangle = \sum_{nn'} e^{i(\epsilon_n^f - \epsilon_{n'}^f)(t-\tau)} n_{nn'}^{i \rightarrow f} U_{nn'}^f U_{mn'}^{f\dagger}. \quad (\text{E15})$$

These expressions are generalized to the case of $(p+1)$ quenches as follows

$$n_{nn'}^{i \rightarrow f} = \sum_{kk'} e^{i(\epsilon_k^Q - \epsilon_{k'}^Q)\tau_p} n_{kk'}^{i \rightarrow Q_p} (U^{Q_p} U^{f\dagger})_{kn} (U^f U^{Q_p\dagger})_{n'k'}, \quad (\text{E16})$$

which is a recursion relation allowing $n^{i \rightarrow Q_p}$ to be derived from $n^{i \rightarrow Q_{p-1}}$, and consequently from $n^{i \rightarrow Q_1}$ determined in E13. Finally, we have for the occupation of the orbitals

$$\langle n_m(t > \tilde{\tau}_p) \rangle = \sum_{nn'} e^{i(\epsilon_n^f - \epsilon_{n'}^f)(t-\tilde{\tau}_p)} n_{nn'}^{i \rightarrow f} U_{nn'}^f U_{mn'}^{f\dagger}, \quad (\text{E17})$$

with $\tilde{\tau}_p = \sum_{i=1}^p \tau_i$.

The formulae above for the real-time dynamics following multiple quenches within ED is without any approximation. The extension to the case of an infinite switch-on time, $\tilde{\tau}_p \rightarrow +\infty$, is obtained straight forwardly by setting $k = k'$ in E16, and yields the time independent long-time limit result for the occupation numbers.

¹ D. C. Langreth and P. Nordlander, *Phys. Rev. B* **43**, 2541 (1991).
² M. Pamperin, F. X. Bronold, and H. Fehske, *Phys. Rev. B* **91**, 035440 (2015).
³ A.-P. Jauho, N. S. Wingreen, and Y. Meir, *Phys. Rev. B* **50**, 5528 (1994).
⁴ E. Sela and Y. Oreg, *Phys. Rev. Lett.* **96**, 166802 (2006).
⁵ A. Schiller and A. Silva, *Phys. Rev. B* **77**, 045330 (2008).
⁶ J. Splettstoesser, M. Governale, J. König, and R. Fazio, *Phys. Rev. Lett.* **95**, 246803 (2005).
⁷ L. Perfetti, P. A. Loukakos, M. Lisowski, U. Bovensiepen, H. Berger, S. Biermann, P. S. Cornaglia, A. Georges, and M. Wolf, *Phys. Rev. Lett.* **97**, 067402 (2006).
⁸ J. K. Freericks, V. M. Turkowski, and V. Zlatić, *Phys. Rev. Lett.* **97**, 266408 (2006).
⁹ J. K. Freericks, H. R. Krishnamurthy, and T. Pruschke, *Phys. Rev. Lett.* **102**, 136401 (2009).
¹⁰ H. Aoki, N. Tsuji, M. Eckstein, M. Kollar, T. Oka, and P. Werner, *Rev. Mod. Phys.* **86**, 779 (2014).
¹¹ J. Bauer, C. Salomon, and E. Demler, *Phys. Rev. Lett.* **111**, 215304 (2013).
¹² Y. Nishida, *Phys. Rev. Lett.* **111**, 135301 (2013).
¹³ Y. Nishida, *Phys. Rev. A* **93**, 011606 (2016).
¹⁴ L. Riegger, N. Darkwah Oppong, M. Höfer, D. R. Fernandes, I. Bloch, and S. Fölling, *Phys. Rev. Lett.* **120**, 143601 (2018).
¹⁵ W. Metzner, M. Salmhofer, C. Honerkamp, V. Meden, and K. Schönhammer, *Rev. Mod. Phys.* **84**, 299 (2012).
¹⁶ D. M. Kennes, S. G. Jakobs, C. Karrasch, and V. Meden, *Phys. Rev. B* **85**, 085113 (2012).
¹⁷ H. Schoeller, *The European Physical Journal Special Topics* **168**, 179 (2009).
¹⁸ D. Lobaskin and S. Kehrein, *Phys. Rev. B* **71**, 193303 (2005).
¹⁹ P. Wang and S. Kehrein, *Phys. Rev. B* **82**, 125124 (2010).
²⁰ G. Cohen, E. Gull, D. R. Reichman, and A. J. Millis, *Phys. Rev. Lett.* **112**, 146802 (2014).
²¹ E. Gull, A. J. Millis, A. I. Lichtenstein, A. N. Rubtsov, M. Troyer, and P. Werner, *Rev. Mod. Phys.* **83**, 349 (2011).
²² U. Weiss, *Quantum dissipative systems*, Vol. 13 (World Scientific Pub Co Inc, 2008).
²³ L. Mühlbacher and E. Rabani, *Phys. Rev. Lett.* **100**, 176403 (2008).
²⁴ A. J. Daley, C. Kollath, U. Schollwöck, and G. Vidal, *Journal of Statistical Mechanics: Theory and Experiment* **2004**, P04005 (2004).
²⁵ S. R. White and A. E. Feiguin, *Phys. Rev. Lett.* **93**, 076401 (2004).
²⁶ P. Schmitteckert, *Journal of Physics Conference Series* **220**, 012022 (2010).
²⁷ C. Schinabeck, A. Erpenbeck, R. Härtle, and M. Thoss, *Phys. Rev. B* **94**, 201407 (2016).
²⁸ C. Schinabeck, R. Härtle, and M. Thoss, ArXiv e-prints (2018), arXiv:1802.09283 [cond-mat.mes-hall].
²⁹ F. B. Anders and A. Schiller, *Phys. Rev. Lett.* **95**, 196801 (2005).
³⁰ F. B. Anders and A. Schiller, *Phys. Rev. B* **74**, 245113 (2006).
³¹ F. B. Anders, *Phys. Rev. Lett.* **101**, 066804 (2008).
³² F. B. Anders, *Journal of Physics-Condensed Matter* **20**, 195216 (2008).
³³ E. Eidelstein, A. Schiller, F. Gütte, and F. B. Anders, *Phys. Rev. B* **85**, 075118 (2012).
³⁴ F. Gütte, F. B. Anders, U. Schollwöck, E. Eidelstein, and A. Schiller, *Phys. Rev. B* **87**, 115115 (2013).
³⁵ H. T. M. Nghiêm and T. A. Costi, *Phys. Rev. B* **89**, 075118 (2014).
³⁶ H. T. M. Nghiêm and T. A. Costi, *Phys. Rev. B* **90**, 035129 (2014).
³⁷ H. T. M. Nghiêm, D. M. Kennes, C. Klöckner, V. Meden, and T. A. Costi, *Phys. Rev. B* **93**, 165130 (2016).
³⁸ H. T. M. Nghiêm and T. A. Costi, *Phys. Rev. Lett.* **119**, 156601 (2017).
³⁹ A. Khedri, T. A. Costi, and V. Meden, *Phys. Rev. B* **96**, 195155 (2017).
⁴⁰ A. Rosch, *The European Physical Journal B-Condensed Matter and Complex Systems* **85**, 6 (2012).
⁴¹ K. G. Wilson, *Rev. Mod. Phys.* **47**, 773 (1975).
⁴² H. R. Krishna-murthy, J. W. Wilkins, and K. G. Wilson, *Phys. Rev. B* **21**, 1003 (1980).
⁴³ C. Gonzalez-Buxton and K. Ingersent, *Phys. Rev. B* **57**, 14254 (1998).
⁴⁴ R. Bulla, T. A. Costi, and T. Pruschke, *Rev. Mod. Phys.* **80**, 395 (2008).

⁴⁵ G. D. Scott, Z. K. Keane, J. W. Ciszek, J. M. Tour, and D. Natelson, *Phys. Rev. B* **79**, 165413 (2009).

⁴⁶ A. V. Kretinin, H. Shtrikman, D. Goldhaber-Gordon, M. Haml, A. Weichselbaum, J. von Delft, T. Costi, and D. Mahalu, *Phys. Rev. B* **84**, 245316 (2011).

⁴⁷ G. D. Scott, D. Natelson, S. Kirchner, and E. Muñoz, *Phys. Rev. B* **87**, 241104 (2013).

⁴⁸ A. Oguri and A. C. Hewson, *Phys. Rev. B* **97**, 035435 (2018).

⁴⁹ G. Cohen, D. R. Reichman, A. J. Millis, and E. Gull, *Phys. Rev. B* **89**, 115139 (2014).

⁵⁰ A. Dorda, M. Nuss, W. von der Linden, and E. Arrigoni, *Phys. Rev. B* **89**, 165105 (2014).

⁵¹ A. Dorda, M. Ganahl, H. G. Evertz, W. von der Linden, and E. Arrigoni, *Phys. Rev. B* **92**, 125145 (2015).

⁵² D. M. Fugger, A. Dorda, F. Schwarz, J. von Delft, and E. Arrigoni, *New Journal of Physics* **20**, 013030 (2018).

⁵³ A. Weichselbaum and J. von Delft, *Phys. Rev. Lett.* **99**, 076402 (2007).

⁵⁴ W. C. Oliveira and L. N. Oliveira, *Phys. Rev. B* **49**, 11986 (1994).

⁵⁵ V. L. Campo and L. N. Oliveira, *Phys. Rev. B* **72**, 104432 (2005).

⁵⁶ Equation (D4) in Weymann *et al*⁶⁵.

⁵⁷ In contrast to the Anderson model, the RLM is a spinless model so within the TDNRG calculations for the latter one can retain a larger number of states than for the former.

⁵⁸ R. Bulla, A. C. Hewson, and T. Pruschke, *Journal of Physics: Condensed Matter* **10**, 8365 (1998).

⁵⁹ The Friedel sum rule for the Anderson impurity model states that $\pi\Gamma A(\omega = 0) = \sin^2(\pi n_d/2)$ where $A(\omega)$ is the zero temperature spectral function⁶⁶. For a particle-hole symmetric final state, the RHS equals 1.

⁶⁰ F. Gütte, *Real time dynamics and critical phenomena of quantum impurity systems*, Ph.D. thesis, University of Dortmund (2013).

⁶¹ W. Hofstetter, *Phys. Rev. Lett.* **85**, 1508 (2000).

⁶² R. Peters, T. Pruschke, and F. B. Anders, *Phys. Rev. B* **74**, 245114 (2006).

⁶³ T. A. Costi, A. C. Hewson, and V. Zlatić, *J. Phys.: Condens. Matter* **6**, 2519 (1994).

⁶⁴ P. Nordlander, M. Pustilnik, Y. Meir, N. S. Wingreen, and D. C. Langreth, *Phys. Rev. Lett.* **83**, 808 (1999).

⁶⁵ I. Weymann, J. von Delft, and A. Weichselbaum, *Phys. Rev. B* **92**, 155435 (2015).

⁶⁶ A. C. Hewson, *The Kondo Problem to Heavy Fermions* (Cambridge University Press, Cambridge, 1997).